JGR Earth Surface

RESEARCH ARTICLE
10.1029/2018JF004819

Seismic Tremor Reveals Spatial Organization and Temporal Changes of Subglacial Water System

Margot E. Vore[1], Timothy C. Bartholomaus[2], J. Paul Winberry[3], Jacob I. Walter[4], and Jason M. Amundson[5]

[1]Department of Geography, University of Idaho, Moscow, ID, USA, [2]Department of Geological Sciences, University of Idaho, Moscow, ID, USA, [3]Department of Geological Sciences, Central Washington University, Ellensburg, WA, USA, [4]Oklahoma Geological Survey, University of Oklahoma, Norman, OK, USA, [5]Department of Natural Sciences, University of Alaska Southeast, Juneau, AK, USA

Abstract Subglacial water flow impacts glacier dynamics and shapes the subglacial environment. However, due to the challenges of observing glacier beds, the spatial organization of subglacial water systems and the time scales of conduit evolution and migration are largely unknown. To address these questions, we analyze 1.5- to 10-Hz seismic tremor that we associate with subglacial water flow, hat is, glaciohydraulic tremor, at Taku Glacier, Alaska, throughout the 2016 melt season. We use frequency-dependent polarization analysis to estimate glaciohydraulic tremor propagation direction (related to the subglacial conduit location) and a degree day melt model to monitor variations in melt-water input. We suggest that conduit formation requires sustained water input and that multiconduit flow paths can be distinguished from single-conduit flow paths. Theoretical analysis supports our seismic interpretations that subglacial discharge likely flows through a single-conduit in regions of steep hydraulic potential gradients but may be distributed among multiple conduits in regions with shallower potential gradients. Seismic tremor in regions with multiple conduits evolves through abrupt jumps between stable configurations that last 3–7 days, while tremor produced by single-conduit flow remains more stationary. We also find that polarized glaciohydraulic tremor wave types are potentially linked to the distance from source to station and that multiple peak frequencies propagate from a similar direction. Tremor appears undetectable at distances beyond 2–6 km from the source. This new understanding of the spatial organization and temporal development of subglacial conduits informs our understanding of dynamism within the subglacial hydrologic system.

Key Points:
- Single-station polarization techniques can be used to analyze seismic tremor produced by sustained water flow through subglacial conduits
- Single-conduit and multiconduit subglacial flow paths appear to be distinguishable through power comparisons of glaciohydraulic tremor bands
- In locations with multiple conduits, changes in water flux undergo abrupt changes between 3- and 7-day periods of relative stability

Supporting Information:
- Supporting Information S1

Correspondence to:
M. E. Vore,
margot.vore@outlook.com

Citation:
Vore, M. E., Bartholomaus, T. C., Winberry, J. P., Walter, J. I., & Amundson, J. M. (2019). Seismic tremor reveals spatial organization and temporal changes of subglacial water system. *Journal of Geophysical Research: Earth Surface*, *124*, 427–446. https://doi.org/10.1029/2018JF004819

Received 19 JUL 2018
Accepted 10 JAN 2019
Accepted article online 18 JAN 2019
Published online 9 FEB 2019

1. Introduction

Hundreds of meters of glacier ice inhibit direct observation of glacier beds and limit our understanding of subglacial landscapes. The interaction between overburden pressure exerted by the glacier on its bed and subglacial water flow creates an annual cycle that transforms the subglacial water system from an inefficient, distributed system in the winter to an efficient, channelized system during the melt season (Chu, 2014; Cowton et al., 2013; Fountain & Walder, 1998). While this annual cycle has been broadly described, the spatiotemporal evolution of subglacial conduits, including their number, location, and potential migration, remains poorly known. Due to the influence that subglacial water flow has on glacier sliding speeds (Bartholomaus et al., 2008; Bartholomew et al., 2010; Iken & Bindschadler, 1986; Willis, 1995) locating and tracking temporal changes of subglacial conduits will likely lead to better constraints on glacier dynamics.

Seismology has the potential to continuously monitor the evolution of the subglacial water system. Terrestrial rivers and streams produce high-frequency (>1 Hz) ambient seismic tremor through turbulent water flow and sediment transport, with lower-frequency tremor signals radiating from turbulent water flow (Burtin et al., 2008; Gimbert et al., 2014; Schmandt et al., 2013, 2017; Tsai et al., 2012). If bedload transport produces these tremor signals, as hypothesized, the seismic power of a given mechanism of terrestrial river tremor is dependent on the source-to-seismometer distance, with seismic tremor sources close to a seismic station (<100 m) recording relatively greater power (Gimbert et al., 2014; Tsai et al., 2012). Flowing water in subglacial conduits also produce seismic tremor, known as glaciohydraulic tremor, which can be used as a proxy for subglacial water flow (Bartholomaus et al., 2015). Glaciohydraulic tremor consists of relatively low-energy seismic waves lasting several days to months in excess of some site-specific, baseline level.

Bartholomaus et al. (2015) found that, at three glaciers in Alaska and one in Greenland, glaciohydraulic tremor occurs between 1.5 and 10 Hz, with the strongest power near 3 Hz.

Due to its long-duration and gradual, emergent onset, there are a limited number of methods capable of locating sources of seismic tremor. Sources of glaciohydraulic tremor produced by moulins have been successfully located using cross correlation and beamforming (Aso et al., 2017) as well as matched field processing methods (Walter et al., 2015). Beamforming (Rost & Thomas, 2002) has also been successfully used to track temporal changes in tremor during transient subglacial floods (Winberry et al., 2009). However, frequency-dependent polarization analysis (FDPA), which was first introduced in Park et al. (1987), is also a viable method for tracking glaciohydraulic tremor. FDPA has been used in various studies (Goodling et al., 2018; Koper & Burlacu, 2015; Koper & Hawley, 2010; Workman et al., 2016) to track locations of microseisms, ambient seismic noise, and hydraulic sources in settings throughout the United States and is unique in that it relies on a single three-component seismometer rather than a tight array of instruments to locate the tremor's source direction. FDPA is particularly useful for analyzing seismic signals with no discernable structure that may have short propagation distances and in situations where the local environment places severe constraints on the design of a seismic network (i.e., inability to deploy tight arrays of instrumentation).

In this paper we apply FDPA (section 3.1.1) to classify glaciohydraulic tremor signals (seismic tremor signals produced by subglacial water flow) on Taku Glacier (section 3.2.1) over the 2016 melt season. We identify variations in the background, slowly varying seismic signals (including glaciohydraulic tremor), analyze the highest power frequencies, define the wave types associated with glaciohydraulic tremor (section 4.1), calculate the back azimuth of these waves to locate tremor sources (section 4.2), and investigate temporal changes in source locations (section 4.3). Using the findings of sections 4.2 and 4.3, we discuss the spatial organization of the subglacial conduits (section 5.1), analyze the rate of conduit evolution (section 5.2), examine the relationship between water input and Rayleigh wave glaciohydraulic tremor (section 5.3), and discuss the properties of glaciohydraulic tremor signals themselves (sections 5.4 and 5.5).

2. Research Site and Instrumentation

To explore the connections between an evolving subglacial hydrologic network and seismic tremor, we collected data at Taku Glacier (~25 km northeast of Juneau, Alaska), one of the thickest temperate valley glaciers in the world, with maximum ice thicknesses of ~1,400 m (Nolan et al., 1995). This glacier is in the advancing phase of the tidewater glacier cycle and has advanced over 7 km since the 1890s due to the filling of Taku Inlet with sediment that has essentially eliminated iceberg calving since the end of the twentieth century (Larsen et al., 2007; Motyka et al., 2006; Post & Motyka, 1995). Large surface melt volumes occur each year on Taku Glacier, with nearly 8.7 m of water equivalent thickness melting from near-terminus locations during our 2016 experiment. Existing subglacial theory predicts that these high melt fluxes should produce an efficient drainage system during the summer months (Cowton et al., 2013; Fountain & Walder, 1998), resulting in the emission of strong glaciohydraulic tremor signals from the glacier's bed (Bartholomaus et al., 2015).

Thirteen three-component, broadband seismometers were deployed in glacier-proximal sediment or 4-m-deep ice boreholes in March 2016, while the snowpack reached up to 4-m thickness. All sensors were recovered in October 2016. Glacier-deployed sensors outside their tilt tolerances, instrumentation failures, power failures, and wildlife damage limited the number of usable stations to seven, each of which suffered from data gaps. All seven of the working seismic stations (Figure 1) were deployed below the glacier's equilibrium line altitude (found near 925 m; Pelto et al., 2008), with the highest elevation station, TWLV (named for the nearby approximately 1,200-m ice thickness, Nolan et al., 1995), at approximately 600-m elevation. Each station consisted of Nanometric Meridian Compact Posthole sensors, with 120-s low-frequency corners and sampled at 200 Hz. Station ETIP (at the east tip of the glacier), RTBD (at a right bend in the glacier), and TWLV were buried just off-ice beneath approximately 15 cm of sediment, and the remaining four seismometers were buried off-ice at a depth of about 1 m. Taku River is located ~0.6 km away from the GIW (abbreviated for the winter deployment of the GeoIce project) station array, located at the southern terminus, and ~1.5 km from station ETIP, which is located on a sandbar in the middle of a shallow outlet stream (<250 m wide) that flows out of the terminus, separating ETIP from the glacier.

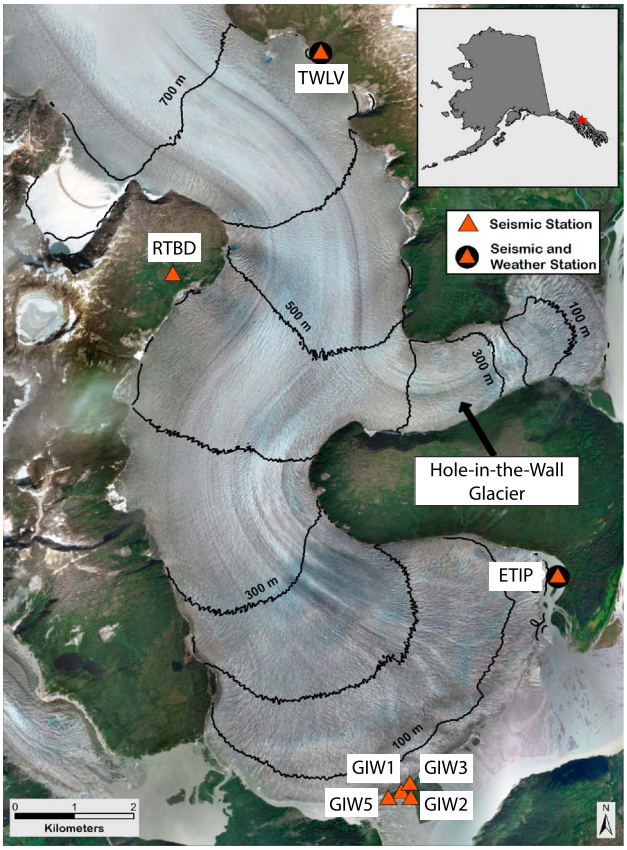

Figure 1. Map of Taku Glacier with the locations of the seven seismic stations (orange triangles) and the two weather stations (black circles). Hole-In-The-Wall Glacier protrudes from Taku Glacier to the east and the Taku River flows parallel to and southeast of the glacier terminus.

Weather stations, colocated with seismic stations ETIP and TWLV (Figure 1), were also deployed during the collection period. Humidity, wind, and temperature were collected at both weather stations using a Vaisala WXT520 sensor that recorded every 10 min. Rain data were collected at ETIP using an Onset HOBO tipping bucket rain gauge, with each tip representing 0.2 mm of precipitation.

3. Methods

3.1. Analysis of Seismic Tremor

3.1.1. Frequency Dependent Polarization Analysis

The configuration of seismic stations at Taku Glacier is designed to track the broad spatial evolution of tremor along the glacier's length throughout the melt season. The tremor we report here has no discernible onset and has no structure at time scales shorter than minutes, which is different than some types of tectonic tremor (Shelly et al., 2007). We apply FDPA (Park et al., 1987) rather than cross correlation, back projection, or beamforming due to its ability to analyze seismic tremor signals without a tight array configuration of seismometers. We use FDPA to determine the wave type, polarization, and back azimuth of glaciohydraulic tremor signals. Additional clarification of this method is provided in Koper and Hawley (2010), Koper and Burlacu (2015), and Workman et al. (2016), who used this method to track spatial variations in ambient seismic noise. A flowchart of the workflow that follows is presented in Figure S1 in the supporting information.

We examine the tremor signals with daily temporal resolution and begin with 1 day of a three-component displacement seismic signal

$$x(t) = [z(t), n(t), e(t)] \tag{1}$$

with z representing the vertical channel and n and e representing the north and east channels, respectively. We remove microseisms from $x(t)$ and subtract the mean and linear trend from the data. The result is then split into 1-min subsets with 50% overlap,

$$x_k(t) = [z_k(t), n_k(t), e_k(t)] \; with \; k \in \{1, ...2879\}, \tag{2}$$

where k represents the subset number. For each channel in subset k, apply a Fourier transform to transform the time domain seismic signal into the frequency domain with a prolate spheroidal taper to reduce spectral leakage, such that

$$x_k(t) \rightarrow X_k(f) = [Z_k(f), N_k(f), E_k(f)]. \tag{3}$$

Each row of $X_k(f)$ represents a different frequency within the signal during a 1-min subset.

For frequency f, a 3×3 spectral covariance matrix, $M_k(f)$, is calculated for each 1-min subset by multiplying the row of $X_k(f)$ associated with frequency f with its conjugate transpose

$$M_k(f) = X_k(f)^H * X_k(f), \tag{4}$$

where k represents the subset number within a given day's record. The spectral covariance matrices representing 1 min of 50% overlapped data for a given frequency are binned into 7-min groups (i.e., 13 consecutive matrices), M_{aj}, where a represents the group number and $j \in \{1, \ldots, 13\}$ represents the matrix's number in group a. An average spectral covariance matrix for each 7-min grouping, $M_a(f)$, is calculated by separately, linearly averaging the real and imaginary components of the 13 matrices in each grouping together. Thus,

$$M_a(f) = \frac{\sum_{j=1}^{13} Re(M_{aj}(f))}{13} + \frac{\sum_{j=1}^{13} Im(M_{aj}(f))}{13} i \tag{5}$$

represents an average 7-min seismic signal at frequency f. Averaging of the 13 spectra in a group prevents short-term transient events or random noise from interfering with back azimuth estimates.

A singular value decomposition of the average spectral covariance matrix,

$$M_a = UDV^H \tag{6}$$

produces left eigenvectors, $U = [U_1, U_2, U_3]$, right eigenvectors, $V^H = [V_1, V_2, V_3]$, and singular values

$$D = \begin{bmatrix} d_1 & 0 & 0 \\ 0 & d_2 & 0 \\ 0 & 0 & d_3 \end{bmatrix},$$

where each component of U and V^H are vectors. Each singular value, d_i, represents the average seismic energy, at a given frequency, within the plane of motion defined by its eigenvector. If $d_1 >> d_2$ and d_3, then ground motion is largely constrained within a single plane of motion, and we define a polarization vector, P,

$$P = V_1^T = \left[A_Z e^{-i\varphi_Z}, A_N e^{-i\varphi_N}, A_E e^{-i\varphi_E}\right], \tag{7}$$

where ${V_1}^T$ is the transform of the first component of V^H. P consists of three complex values that contain both amplitude (A_i) and phase (φ_i) components. The real and imaginary components of the vector span the waveform's dominant plane of motion.

To determine the wave type associated with the average 7-min seismic signal, the phase lag between the horizontal and vertical components, φ_{VH}, is calculated. The phase of the horizontal components, φ_H, is equal to

$$\omega t = -\frac{1}{2}\arg\left((A_N e^{-i\varphi_N})^2 + (A_E e^{-i\varphi_E})^2\right) + l\pi/2 \text{ where } l \text{ is an integer} \tag{8}$$

that maximizes

$$A_H = \left[(A_N \cos(\omega t + \varphi_N))^2 + (A_E \cos(\omega t + \varphi_E))^2\right]. \tag{9}$$

Equations (8) and (9) thus determine the dominant direction of horizontal motion.

Once φ_H is determined, the lag between horizontal and vertical components is calculated

$$\varphi_{VH} = \varphi_H - \varphi_z, \tag{10}$$

where the phase of φ_{VH} is bounded between −90° and 90°, with $\varphi_{VH} > |90°|$ equivalent to $\varphi_{VH} + \pi$. A phase lag between the horizontal and vertical component that is close to 0 represents a body wave with linear particle motions, whereas $|\varphi_{VH}| = 90°$ is indicative of a Rayleigh wave with elliptical particle motions (e.g., Workman et al., 2016). We then bin these phase lags for each 7-min group by wave type (i.e., Rayleigh wave, body wave, or mixed wave) and use them to calculate the percentage of waveforms consistent with each category for a given day. We elaborate on this in section 3.1.2.

Once the polarization vector has been identified, we calculate the back azimuth, θ, of the waveform

$$\theta = \tan^{-1}\left(\frac{A_E}{A_N}\right). \tag{11}$$

FDPA can only determine back azimuths of Rayleigh waves due to their distinct elliptical (rather than rectilinear) motion. By calculating a back azimuth for each 7-min group, we calculate a daily probability distribution for the back azimuth of Rayleigh wave tremor by binning all estimates for a given frequency into 5° bins and determining the number of estimates in each bin.

3.1.2. Classification of Glaciohydraulic Tremor

Before calculating back azimuths of glaciohydraulic tremor seismic waves, we apply three constraints to identify the frequencies and time periods containing tremor locatable via the FDPA approach (section 3.1.1). First, we require that glaciohydraulic tremor be present as a peak in seismic power associated with subglacial water flow (Bartholomaus et al., 2015). Second, we require glaciohydraulic tremor be strongly polarized (i.e., particle motions well constrained within a dominant plane of motion), and third, the tremor must be predominantly composed of Rayleigh waves. FDPA cannot locate the wave propagation direction without the second and third constraints. Within a seismograph, all three of these criteria must hold true for frequencies to contain locatable glaciohydraulic tremor. We further describe the implementation of these criteria in the following paragraphs.

The first constraint to identifying glaciohydraulic tremor frequencies is that seismic power must be unusually strong in a given frequency band and be persistent across multiple days. Glaciohydraulic tremor frequency bands contain power peaks that begin early in the melt season and progressively intensify throughout the summer months, due to the gradual formation and growth of subglacial conduits that move large volumes of water (Bartholomaus et al., 2015; Gimbert et al., 2016). Thus, we consider high-power frequency bands that emerge in the spring and persist throughout the melt season to be hallmarks of glaciohydraulic tremor. Median power spectrograms, created by finding the median power spectral density of 20-s data samples within 1-hr waveform subsets, allows for the identification of frequencies that contain these patterns, while reducing the potential impact of crevasse-produced icequakes or other seismic transients that are short lived (Bartholomaus et al., 2015). For the purposes of describing tremor power, we focus our analysis and discussion on the seismic data's vertical channel.

We determine which frequencies exhibit peaks in seismic power by analyzing a smoothed daily power spectral density of vertical ground motion. To find the frequencies that exhibit a peak in seismic power, the power differences, D_1 and D_2, between the power value γ at frequency f, and its two surrounding local minimum power values, m_1 and m_2, are calculated and compared to a threshold value, D_t (Figure S2). We assign this threshold value D_t to the fiftieth percentile difference between consecutive local minimum and maximum values between 1.5 and 10 Hz during the last 2 weeks of reliable seismic signal at a given station (typically the first 2 weeks of July) to ensure that the subglacial conduits and any tremor signals are well developed (at their greatest melt season values, see section 3.2). The threshold value is calculated using the 1.5- to 10-Hz frequency range as it encompasses the majority of seismic power peaks visually identified in each station's median power spectrogram. This method allows a different threshold value for each seismic station to compensate for varying ranges of seismic power at each collection site. If D_1 and D_2 both exceed the threshold value D_t of a respective station, then we consider frequency f to contain a peak in seismic power (Figure 2a).

For FDPA to calculate back azimuths of glaciohydraulic tremor, frequencies that contain tremor must also be strongly polarized. Waveforms with strong polarization contain a large proportion of their total seismic energy within a single plane of motion, which indicates an organized seismic signal and coherent arrivals (presumably from a single direction). The extent of wave polarization is determined by the ratio between the first and second singular values of the waveform (equation (6)), where frequencies with a ratio greater than 2.5 are considered to be strongly polarized (Figure 2b). The threshold value of 2.5 was selected as it encompasses qualitatively identified polarization peaks while excluding minima in polarization values at all stations except ETIP (which has unusually large polarization values). A polarization threshold value of 3 begins to exclude qualitatively identified local maxima in ratio values, while a polarization threshold of 2 is too inclusive of local minima in the polarization values.

Finally, for FDPA to resolve back azimuths, glaciohydraulic tremor frequencies must have a consistent phase lag between the waveform's horizontal and vertical planes of motion that are indicative of Rayleigh waves. Peaks in wave type are identified by comparing the daily percentage of 7-min signal subsets of a given phase lag to a threshold value, with phase lags categorized into three groups: Rayleigh waves, body waves, and mixed waves. The percentage of waveforms in a given category is determined by binning the phase lags produced by FDPA for a given frequency over 1 day into one of the three wave type categories and calculating the percentage of time windows that are Rayleigh waves, body waves, or mixed waves. For classification purposes, we define Rayleigh waves as having an absolute phase lag between 70° and 90° (signifying well-defined elliptical particle motion) and body waves having 0° to

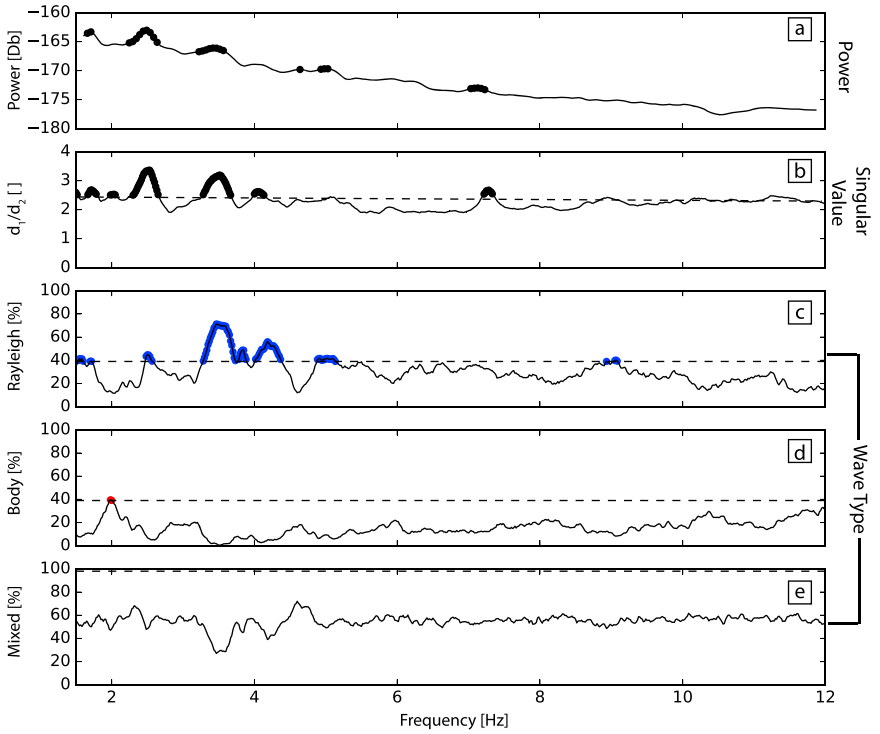

Figure 2. Representation of the frequency-dependent glaciohydraulic tremor constraints at seismic station RTBD on 4 July 2016. (a) Power peak constraint with the power being relative to $(m/s)^2$ / Hz. The bold lines represent the peaks in power and the thin black line is the smoothed median vertical PSD for 4 July at RTBD. (b) Wave polarization constraint. Bold segments represent wave polarization ratios that exceed the 2.5 threshold (represented by the dashed line). (c–e) Wave type constraint with each panel representing one of three categories: (c) Rayleigh waves, (d) body waves, and (e) mixed waves. The threshold value for peaks in Rayleigh waves and body waves is 39%, and the threshold value for mixed waves is 98%, with the thresholds being represented by the dotted line. The colored lines represent the frequencies that exceed the threshold value. The frequencies where all three of these constraints hold true are those that contain locatable glaciohydraulic tremor.

20° absolute phase lag (signifying rectilinear motion). While Love waves also exhibit rectilinear motion, our signals display high power in the vertical direction suggesting *P* or *SV* seismic waves occur rather than Love waves. We define mixed waves as those that do not fall into the other two categories, with a 20° to 70° absolute phase lag.

The threshold value for wave type peaks is found by comparing an unclassifiable waveform (one with a random distribution of phase lags, in which each phase lag has the same probability of occurring) to the actual waveform distribution for a given day. If the percentage of signal subsets of an identified waveform (Rayleigh, body, or mixed) for a given day and frequency is 75% greater than what is expected in a randomly distributed sample, then a waveform peak occurs. Again, this threshold value was chosen on a qualitative basis, through repeated comparison between threshold peaks and visually identifiable peaks at the majority of seismic stations, with higher threshold values excluding peaks in wave type and lower thresholds including unexceptional, low percentages. If a waveform is unclassifiable during a given day (i.e., if the phase lags are randomly distributed), we expect 22% of the waveform subsets to be categorized as Rayleigh waves, 22% to be categorized as body waves, and the remaining 56% of the subsets to be mixed waves. If threshold values are 75% greater than the expected value, then the threshold percentage for body waves and Rayleigh waves is 39% and the mixed wave threshold is 98% (Figures 2c–2e).

It should be noted that all threshold values that are calculated for these three criteria may be considered a conservative estimate for identification of the highest-quality glaciohydraulic tremor signals. There is likely be more intermediate-quality or less well-polarized glaciohydraulic tremor that could be further studied by other techniques.

3.2. Water Input Estimation

To analyze the relationship between glaciohydraulic tremor and subglacial water flow, estimates of daily water input to the subglacial water system are needed. We calculate daily melt using a degree day melt model (Hock, 2003)

$$M = \begin{cases} DDF \sum T\Delta t, T>0 \\ 0, T\leq 0 \end{cases}, \tag{12}$$

where T represents the average temperature at a given location over a time span Δt and DDF is the degree day factor, which differs depending on snow or ice cover.

We extrapolate air temperature measured at ETIP and TWLV across the glacier surface using an empirically determined lapse rate from differences between temperatures at the two stations. A 5-m digital elevation model (DEM) of Taku Glacier collected by IfSAR in 2012–2013 (Fugro EarthData, Inc) is used and resampled to 25 m. The DEM is clipped to the glacier's extent from the Randolph Glacier Inventory (Kienholz et al., 2015). The distributary glacier Hole-In-The-Wall (Figure 1) is removed under the assumption that it contributes no melt to Taku Glacier's subglacial water system. The daily median temperatures are extrapolated to all grid cells of the DEM

$$T_x = (H_x - H_E)\left[T_E + \frac{T_W - T_E}{H_W - H_E}\right], \tag{13}$$

where T represents temperature, H represents elevation of the grid cell, subscripts W and E represents weather station TWLV and ETIP, respectively, and subscript x represents the grid cell of interest. Due to rodent damage to the weather station at TWLV, temperatures are estimated after 28 June using adiabatic cooling rate estimates (found using the temperature differences between the two weather stations and humidity prior to TWLV's malfunction) and temperatures at ETIP.

DDFs and daily snow line elevation are also needed for the degree day melt model. We apply DDFs from Alforbreen Glacier, Sweden, to Taku Glacier due to their similar latitudes and proximities to the coast (Hock, 2003). We choose a DDF for snow of 4.5 mm·day^{-1}·°C^{-1} and a value for ice of 6 mm·day^{-1}·°C^{-1}. The transient snow line between snow- and ice-covered areas is estimated using five clear sky Landsat 7 and 8 images between April and October. We linearly interpolate the daily snow line elevation for days between measured snow line elevations.

Since glaciohydraulic tremor is produced by water flow past a given location in the subglacial water system, we assume water inputs at elevations lower than a measurement's location do not contribute to the tremor signal recorded at each station. Thus, we produce separate melt estimates (in millimeters of water equivalent) for ETIP, RTBD, and TWLV, since each station would plausibly observe glaciohydraulic tremor at a different elevation. GIW stations are excluded from the melt estimates considering most of the tremor bands at these stations point off glacier, signifying that the tremor observed there is not due to subglacial water flow (sections 4.2 and 4.3). We also assume that ice melt is the only melt that contributes to water input and that ice melt is not stored englacially before entering the subglacial water system. Although snowmelt just above the snow line likely contributes to the subglacial water system, we expect that most meltwater from snow either refreezes as it percolates through the snowpack or is otherwise stored in a densifying snowpack in the majority of the glacier's accumulation area (Pelto et al., 2008). Due to our inability to specify the elevation at which snowmelt storage in the snowpack stops, we omit it all together.

To complete the estimate of water input into the subglacial water system, we also include precipitation in our water input model. For days where precipitation fell, we assume that the rain totals recorded at ETIP are representative of rainfall over the area of the glacier where the lapse rate predicted temperature is above 0 °C. Consistent with our handling of snow/ice melt, we exclude water inputs from precipitation that falls on grid cells above the snow line elevation.

These estimates of ice melt and precipitation provide us with a minimum, daily water input to the glacier and allow us to look at commonalities between ice melt and tremor. While the true magnitude of subglacial discharge may differ from our estimate, we expect that the temporal fluctuations in subglacial discharge are captured accurately by our model.

4. Results

4.1. Spectral and Temporal Tremor Characteristics

We observe that seismic tremor signals from this glacier vary slowly, apparently in response to hydrologic variations, do not consist of discrete icequakes and are not particularly correlated with glacier velocity nor weather. Observations of the glacier's surface through satellite imagery and fieldwork show no significant moulins present within our study area, allowing us to conclude that the tremor's source is not a moulin. Median power spectrograms between 0 and 50 Hz from all seismic stations on Taku Glacier reveal that glaciohydraulic tremor occurs in distinct frequency bands that emerge out of the background noise during middle-to-late spring, with power increasing as the melt season progresses. The most defined bands of tremor on the glacier occur between 1.5 and 10 Hz, with microseisms dominating the frequencies below 1.5 Hz, which is consistent with the findings of Bartholomaus et al. (2015). The frequencies that contain these tremor bands exhibit diurnal peaks in power that occur around 4 p.m. Alaska Daylight Time (Figure S4). While these diurnal peaks occur near the time of peak daily melt on Taku Glacier, they likely occur slightly prior to peak subglacial discharge due to routing delays in the water system. These diurnal peaks appear consistent with tremor produced by flowing melt water.

Estimates of tremor frequency and wave type for all seven seismometers on Taku Glacier also depict the multiple distinct frequency bands of locatable tremor that are observed in the median power spectrograms, each of which have a defining wave type (Figure 3). We define a band of locatable tremor as a frequency containing a tremor signal meeting the criteria outlined in section 3.1.2 for at least 4 days during the seismic record. This 4-day constraint prevents short temporal-scale events from being classified as glaciohydraulic tremor, as this type of tremor is expected to occur over week to month time spans (Bartholomaus et al., 2015).

We find that all stations except RTBD experience bands of both body wave and Rayleigh wave dominated frequencies within the 1.5- to 10-Hz frequency range, with all bands of tremor spanning less than 1 Hz (Figure 3). The 4.0- to 4.5-Hz frequency band at ETIP and the 2.1- to 2.4-Hz band at GIW5 experience wave type changes throughout the record and some tremor bands decrease in frequency throughout the melt season, such as the 7.0- to 7.65-Hz band at ETIP (Figure S3). We also find that bands of glaciohydraulic tremor do not start at the same time during the melt season at each of the stations. For instance, the bands of Rayleigh wave glaciohydraulic tremor at RTBD start on 22 June, while Rayleigh wave tremor bands at ETIP begin earlier in the melt season on 1 June (Figure S3). We refer to the start day of sustained tremor meeting our three criteria as the date of tremor initiation.

4.2. Back Azimuths of Glaciohydraulic Tremor

Back azimuth probabilities (Figures 4a–4c) allow us to estimate the direction toward the source or sources of polarized, Rayleigh wave glaciohydraulic tremor. At RTBD, the two bands of Rayleigh wave glaciohydraulic tremor (2.35–2.7 and 3.2–3.7 Hz; Figure 3) come from the southeast, with the highest probability back azimuths for both frequency ranges around 135° (Figure 4b). We see the highest probability back azimuths for the multiple bands of Rayleigh wave glaciohydraulic tremor at ETIP (Figure 4c) coming from a southwesterly direction of about 240°. The tremor band at TWLV has a bigger range of high probability back azimuths with the highest probabilities centered at 180° (Figure 4a). The probability range, as specified by the color ramp in Figures 4a–4c, is similar at stations RTBD and TWLV, both having an average maximum probability of 0.16 over the duration of the record. This probability signifies that 16% of the tremor signal at a given frequency fall within a specified 5° back azimuth bin (if the back azimuths were evenly distributed, 1.4% of the signals within each frequency band would occur from each back azimuth). ETIP exhibits much higher probability values (Figure 4c) with an average maximum probability of the record being 0.52. The probabilities of the polarized, Rayleigh wave glaciohydraulic tremor source directions are then mapped (Figure 4d) with glaciohydraulic tremor sources at ETIP, RTBD, and TWLV coming from Taku Glacier. Multiple-tremor frequency bands at a given station appear to come from similar directions. We find that there is a lot of scatter in the glaciohydraulic tremor source locations at the GIW stations (not shown), with back azimuths pointing in multiple directions with no distinct pattern.

4.3. Temporal Variations in Glaciohydraulic Tremor

Day-to-day comparison of polar plots (such as those in Figures 4a–4c) allows us to visualize significant changes to source probabilities of polarized Rayleigh wave glaciohydraulic tremor as well as track

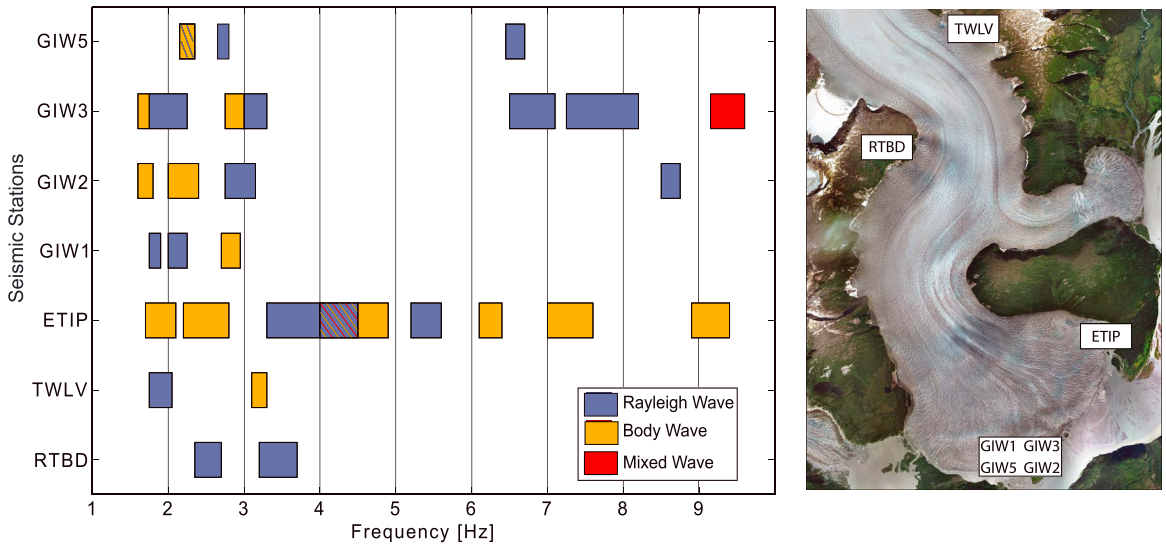

Figure 3. Polarized, glaciohydraulic tremor frequencies by wave type for seismic stations around Taku Glacier (mapped at right). The *y* axis represents the seven seismometers, and each box spans the frequency range of a polarized, glaciohydraulic tremor band with the color specifying the dominant wave type. Striped boxes indicate frequencies that experience a change in the dominate wave type as the melt season progresses.

frequency fluctuations throughout time at a given station. Movies S1–S3 show changes in the frequency and probability of glaciohydraulic tremor source locations at RTBD, ETIP, and TWLV over the melt season by combining polar plots of consecutive days. Movie S1 shows slight day-to-day fluctuations in probabilities and frequencies of tremor at RTBD between 20 June and 17 July; however, no obvious, monotonic changes occur, and back azimuth estimates remain near 135°. Movie S2 shows similar results at ETIP between 1 June and 8 July with back azimuths consistently around 248.

We find that the back azimuth estimations at ETIP (Figure 5b) between the 25th and 75th percentiles cover a smaller range of values than those at RTBD (Figure 5a), with the average range of back azimuth measurements at ETIP being between 6° and 8° and the average range of back azimuths at RTBD being 25° and 28°. Both RTBD and ETIP experience day-to-day changes in median back azimuths over the melt season, with the median back azimuth at RTBD fluctuating by 14° and 21° and 13° and 14° at ETIP. While these fluctuations in back azimuth are similar at both stations, we have more confidence in the back azimuth changes at ETIP because they are nearly double the interquartile range of measurements. Median back azimuths at RTBD also appear to show systematic changes; however, these changes are less than the interquartile range (25°–28°) observed in a single day and therefore cannot be considered significant. Sustained, locatable tremor only emerged at TWLV toward the last few days of our experiment; thus, we do not consider temporal variations in back azimuth direction observed at TWLV. We also disregard the GIW stations at the terminus of Taku Glacier from the analysis due to the scarcity of tremor signals that come from the glacier. We find that only one fourth of the tremor signals at all the GIW stations come from the northwest, in the direction of the glacier, with the remainder of tremor bands propagating from directions of surrounding rivers, meaning they are not glaciohydraulic tremor.

5. Discussion

5.1. Spatial Organization of the Subglacial Water System

The spatial organization and temporal evolution of subglacial conduits is one of many unknowns in glacier hydrology. Daily, median power comparisons of glaciohydraulic tremor at different frequencies (Figure 6) and time series analysis (Figure 5) provide insight into this spatial organization on Taku Glacier. Figures 6b and 6c show the relationship between daily median power estimates within three different frequency bands of glaciohydraulic tremor at ETIP, calculated by taking the median of all power values within a given frequency range. We find that, while these powers are correlated, they experience scatter during the latter part of the melt season and that power within the 4.0- to 4.5-Hz band is nearly 10 times higher than power in other tremor frequency bands at ETIP. These findings reveal that ETIP tremor at different

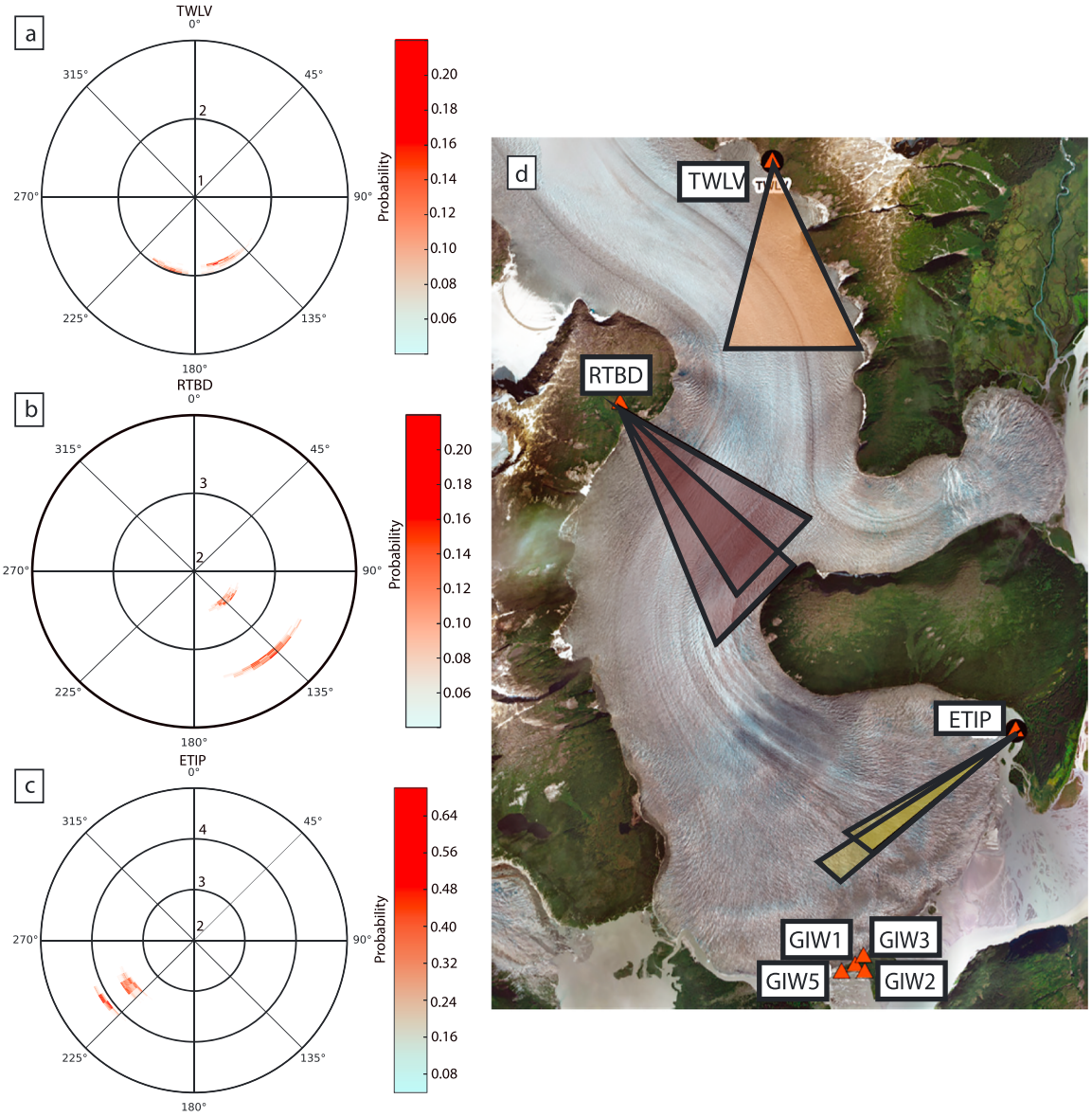

Figure 4. Back azimuth estimations for polarized, Rayleigh wave glaciohydraulic tremor. (a–c) Probability of back azimuth locations for polarized, Rayleigh wave glaciohydraulic tremor signals at station (a) TWLV on 14 September, (b) RTBD on 4 July, and (c) ETIP on 4 July. Back azimuths are defined clockwise from north (0°). Radii on the polar plot denote frequencies, with increasing radii signifying an increase in frequency values. The color ramp depicts the probability of a waveform's source location per frequency with darker reds representing higher probabilities. (d) Map of back azimuth directions at stations on Taku Glacier that correspond to back azimuth probabilities depicted in (a)–(c). Each triangle represents a different polarized, Rayleigh wave glaciohydraulic tremor frequency band, with the width of a triangle representing the range of back azimuth estimates between the 25th and 75th percentiles of measurements for the day. The length of a triangle is arbitrary.

frequencies is affected in contrasting ways by subglacial water flow, suggesting that tremor within these different frequency bands is produced through distinct mechanisms. One possible explanation for the scatter in power relationships is that more than one conduit is conveying subglacial water at ETIP and that each of these conduits produce power at different characteristic frequencies (perhaps dependent on their shape and the size of obstacles within the flow; Gimbert et al., 2014; Tsai et al., 2012). The flux of water through each of these conduits is conceivably independent, such that power within one frequency band could change in ways that are distinct from power changes in a different frequency band.

In contrast with those at ETIP, the median power of different glaciohydraulic tremor bands at RTBD are nearly perfectly correlated ($R^2 = 0.98$, Figure 6a). This suggests that both bands of tremor are produced by

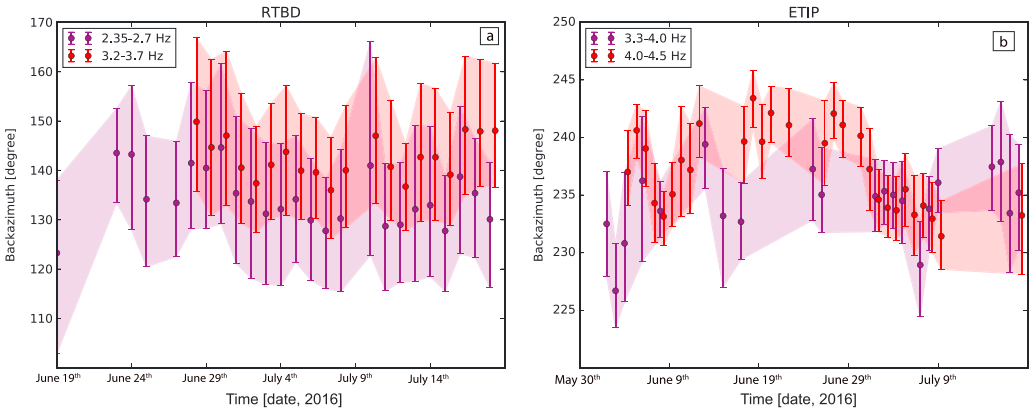

Figure 5. Time series of back azimuth estimations for (a) RTBD and (b) ETIP. Colors represent different frequency band of Rayleigh wave glaciohydraulic tremor. The dots represent the median back azimuth for a given day within a frequency band, while the error bars represent the 25th and 75th percentiles of estimates. The envelopes trace the 25th and 75th percentiles.

a single source, with the frequency bands being identically influenced by subglacial water flow. The subtly different back azimuths between the two frequency bands at RTBD (Figure 4b) are potentially produced by different portions of the same conduit, consisting of different sizes and shapes of obstacles.

Both the across-flow and the along-flow shapes of the Taku Glacier bed offer potential explanations for the difference between the posited single-channel flow at RTBD and multichannel flow at ETIP. Ice thickness soundings are limited to several transverse and longitudinal profiles through our study area (Motyka et al., 2006; Nolan et al., 1995), which are insufficient for the construction of a complete DEM of the glacier bed. As such, we cannot comprehensively map the hydraulic potential field (or its gradient). However, the available cross sections enable us to distinguish between two fundamentally different hydropotential regions: one, a region with steep lateral hydraulic gradient of about 2,000 Pa/m at locations near RTBD and TWLV and a bed sloping down in the direction of glacier flow and two, a region within a few kilometers of the glacier terminus (near ETIP) with nearly flat lateral gradients and an adversely sloped bed that slopes up against glacier flow (Motyka et al., 2006; Nolan et al., 1995; Figures S5 and S6). Steep, lateral potential gradients tend to produce channelized flow that is constrained to the deepest portion of the valley floor, while flow across a flatter hydraulic potential surface can spread out across the landscape in delta-like flow patterns (Shreve, 1972). This envisioned, distributed water flow at ETIP mimics the broadening, distributed ice flow of the glacier terminus. Observations from around the glacier's terminus also support the hypothesis of a delta-like subglacial water system under the terminus with water discharging during the 2016 summer from multiple locations near the toe rather than from a single, dominant outflow stream (Figure 1).

The change in longitudinal gradients (a normal, downward-sloping bed near RTBD and TWLV and an adverse-sloping glacier bed that rises nearly 100 m within 1.5 km of the toe) also promotes a switch from a single-channel system higher up on a glacier to a multiconduit water system near the terminus. As the bed becomes adverse to flow, flow velocity decreases leading to the deposition of sediment (Creyts et al., 2013), thus creating an environment in which delta-like flow occurs. Flowers (2008), who modeled potential subglacial flow patterns, found that adverse bed slopes tend to slow the drainage of water through a less efficient drainage system. Flowers (2008) also found that the substrate of the glacier bed affects drainage system patterns, with flow over hard bedrock forming more channelized and more efficient drainage systems than when forming over sediment-dominated beds. The current terminus of Taku Glacier lies upon a large quantity of eroded sediment that fills the former Taku Inlet (Motyka et al., 2006), whereas up-glacier the bed is likely composed of harder substrates. Therefore, the transition from bedrock to sediment beds may additionally promote the transition from efficient, single-channel water flow up-glacier to a slower draining delta-like flow pattern near the terminus.

In contrast to the model of Flowers (2008), most models of subglacial water flow do not consider adverse bed slopes or heterogenous bed composition and predict patterns of subglacial water flow that progressively concentrate within fewer and fewer large conduits that flow at lower and lower pressure (Hewitt, 2011;

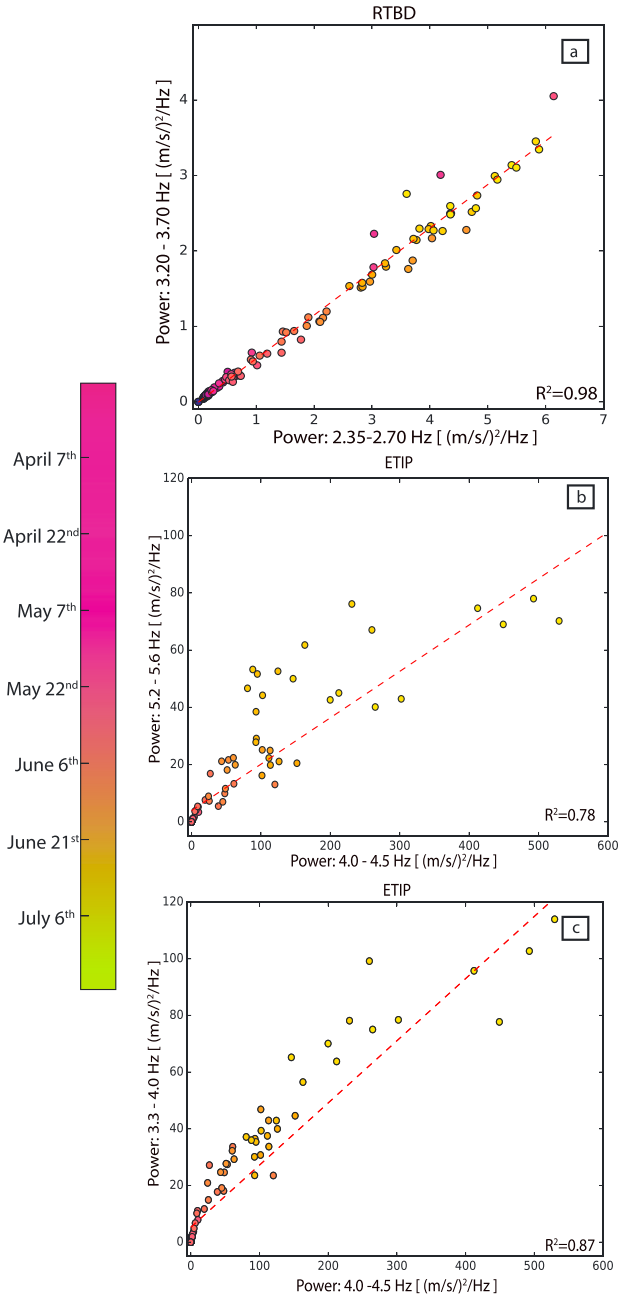

Figure 6. Temporal changes in median power correlations between different frequency bands of glaciohydraulic tremor. Each axis represents the median power of a given frequency band, and each observation represents the daily median power with the color ramp representing the temporal progression of the 2016 melt season. The red dotted line represents the line of best fit with the R^2 value located in the bottom right-hand corner of each frame. (a) Station RTBD with power scaled by 10^{-17}. (b, c) Station ETIP with power scaled by 10^{-15}.

Schoof, 2010; Werder et al., 2013). To examine the theoretical dependence of conduit water pressure on bed slope, we solve the conduit evolution equations of Werder et al. (2013) for the basal water pressure over the last 1.5 km of the Taku Glacier terminus. The Werder et al. (2013) equations evolve the conduit cross-sectional area in response to wall melt, viscous creep closure, and melt or freeze-on (based on the pressure dependence of the freezing point of water). Under steady state conditions and for a fixed ice surface slope, we find that basal water pressure as a percent of overburden increases as the adverse bed slope is increased (i.e., as water flows out of a greater basal overdeepening). Near the conditions encountered at Taku Glacier, where the bed slopes 0.053 (Motyka et al., 2006), for each percent increase in bed slope, the steady state water pressure increases by 5.9% of overburden (Figure S7a). Put another way, conduits along deeper beds are expected to run at higher head pressure (Figure S7b). Thus, as basal conduits encounter a location with an adversely sloped bed, water will encounter a head gradient forcing flow laterally toward locations with shallower beds, where the adverse bed slope is less severe. Water flow is thus expected to be distributary in the presence of adverse bed slopes rather than tributary as is more typical.

The observed transition toward multiple channels at Taku Glacier represents a benchmark for interpreting results of these subglacial hydrologic models. Additional details of this structure could be resolved by installation of a seismic network with greater density than that described here. Stations deployed in small arrays with apertures of 1 km or less would enable us to observe the same conduit source from more than one site and better constrain transitions within the subglacial hydrologic system. Our observations, which are contrary to the prevailing conceptualization of subglacial water flow, represent progress toward understanding the full spectrum of conditions at glacier beds.

5.2. Temporal Scales of Conduit Evolution

The rate at which subglacial conduits respond to changing water inputs is another broad unknown in glacier hydrology. Tremor initiation dates at each station (i.e., the day that all three tremor constraints are first met for a multiday period in a specific frequency range; Figures 7a–7c) can be compared to the varying, estimated water inputs and power fluctuations to understand the time scales of conduit evolution. Changes in glaciohydraulic tremor power are broadly similar to changes in water inputs (Figures 7a and 7d), with seismic power consistently increasing prior to tremor initiation. However, we observe that glaciohydraulic tremor lacks strong polarization or clear retrograde elliptical particle motions until water inputs are sustained at some midsummer level, making early season tremor signals nonlocatable through FDPA.

While seismic power consistently increases prior to tremor initiation at both ETIP and RTBD, consistent median power interrupted by several multiday power peaks occurs for a month prior to the initiation of sustained, polarized, Rayleigh wave, glaciohydraulic tremor at TWLV. While high-powered Rayleigh wave seismic signals are present at TWLV prior to the tremor initiation date of 22 August, our polarization metric remains below the threshold ratio of 2.5. Thus, particle motion at TWLV, while exhibiting Rayleigh wave elliptical motion and high amplitudes, is not concentrated within a single plane of motion until late in the melt season. Sustained, nonpolarized seismic tremor that gradually becomes polarized, which occurs at TWLV, may identify a progressive focusing of turbulent subglacial water flow. Potential explanations include either a distributed water

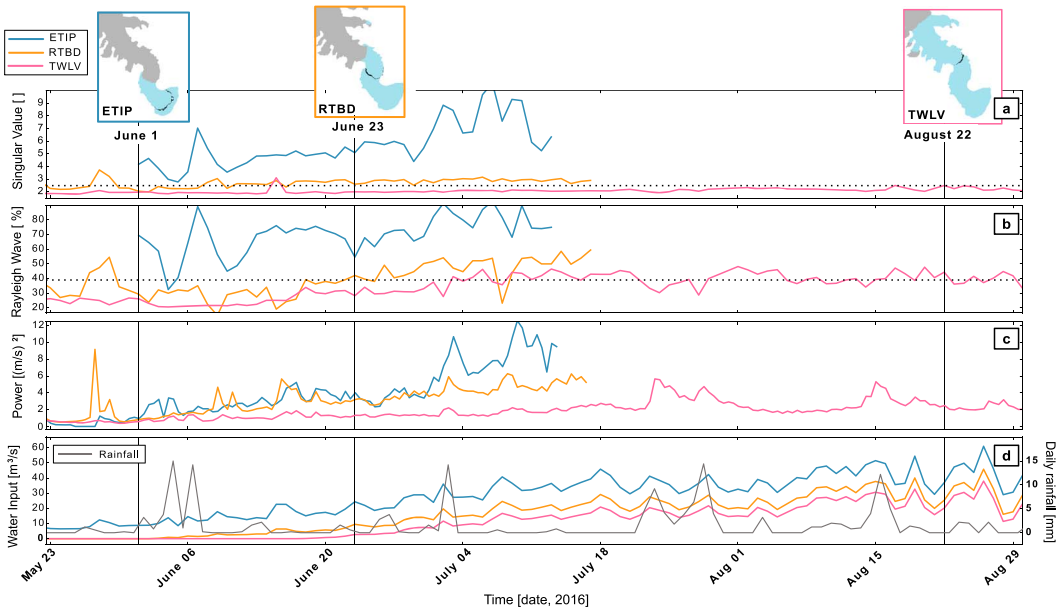

Figure 7. Comparison between tremor initiation (vertical black lines), snow-ice interface location, median seismic power, water input and rain events, and singular value constraint and Rayleigh wave constraint. (a) Time series of singular value constraint with dotted line representing the 2.5 threshold for locatable tremor. (b) Time series of Rayleigh wave constraint with the dotted line representing the 39% threshold for locatable tremor. (c) Median of daily median power at three seismic stations, ETIP, RTBD, and TWLV, within specific frequency ranges of tremor: 3.3–4.0 Hz for ETIP, 2.35–2.70 Hz for RTBD, and 1.75–2.05 Hz for TWLV. Powers at RTBD and TWLV are scaled by 10^{-17}, and ETIP power is scaled by 10^{-14}. (d) Estimated daily water input and daily rainfall (gray line); water input is the sum of estimated melt and rain. (map insets) Snow-ice interface elevation location in relation to average tremor elevation location as determined by back azimuth estimations on the date of sustained tremor initiation. Gray shading represents snow cover on the identified day, blue shading is ice cover, and the black line represents the average elevation of tremor location in proximity to each station. The date under each map inset is the day sustained polarized Rayleigh wave glaciohydraulic tremor began.

system with high water fluxes that progressively forms into a single-conduit throughout the melt season or a single, linear subglacial conduit with a near-uniform distribution of flow obstacles (e.g., boulders that generate high amplitude turbulence along several kilometers of conduit length) that gradually get concentrated into a single boulder jam through sediment transport processes. Such course-grained sediment transport with attendant focusing of tremor generation has been observed at subaerial streams (Roth et al., 2017).

While brief, high-amplitude water input events, such as rain or high melt days, occur throughout the record at all stations, they do not occur at the initiation of polarized, Rayleigh wave, glaciohydraulic tremor. This implies that transient increases in water input are insufficient on their own to form seasonally sustained subglacial conduits that produce locatable glaciohydraulic tremor. On the days of polarized, Rayleigh wave, glaciohydraulic tremor initiation, the snow-ice interface on Taku Glacier is 200–300 m above the elevation of the station recording tremor (Figure 7, map insets), suggesting that tremor initiation does not occur until the snow line has significantly retreated past the elevation at which tremor is recorded (>4 km). We find that at least 20 days of sustained ice melt above the elevation of the seismic stations occurs prior to tremor initiation. In the week prior to the start of sustained tremor at both ETIP and RTBD, subglacial water flow rates (as estimated from the degree day melt model) past the elevation of the seismic station exceed 4 m^3/s, while TWLV observes much higher sustained water flow of 18 m^3/s in the week prior to tremor initiation.

Sustained water input prior to the initiation of polarized, Rayleigh wave, glaciohydraulic tremor, as well as the lack of correlation between transient water input events and tremor initiation, leads to the assumption that some cumulative volume of water input is essential for conduit formation. This finding is supported by Schoof (2010), who suggested that some threshold discharge value is required for conduit development.

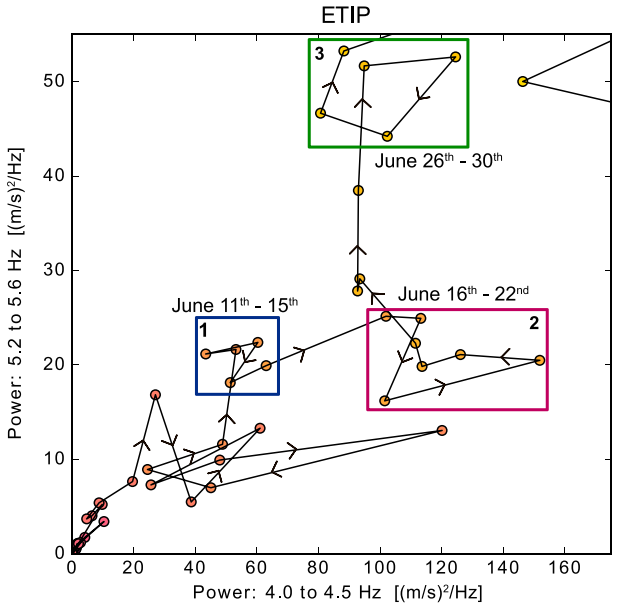

Figure 8. Multiday clustering of median seismic power (a subset from Figure 6b). The x an y axis are scaled by 10^{-15} power. Boxes enclose consecutive days with a consistent power relationship between the two frequency bands, with the dates representing the days where clustering occurs. The power of different glaciohydraulic frequency bands at ETIP are represented on each axis. Arrows indicate the direction of power changes over consecutive days.

Another unknown in subglacial hydrology is the temporal scale of subglacial conduit migration and change. In low hydraulic gradient areas, where we suggest multiconduit flow exists due to scatter in median power comparisons (section 5.1), we see multiday changes in back azimuth measurements (Figure 5b). These back azimuth fluctuations are likely to indicate changes in the source locations. We hypothesize that this phenomenon occurs due to peak water discharge alternating between neighboring conduits, movement of in-conduit water flow obstructions, or other factors that alter the back azimuth of the highest-amplitude glaciohydraulic tremor signals. Tremor-generating locations appear stable for a period of several days before shifting to a new location.

To explore the temporal scale of conduit change, we analyze the relationships between power within different tremor bands of ETIP (Figure 6) in greater detail (Figure 8). We find multiday periods where tremor power at different frequencies are relatively stable (boxes 1–3 of Figure 8), punctuated by abrupt changes. As time progresses from box 1 to box 2 within Figure 8, we see a transition through which power increases in the 4.0- to 4.5-Hz frequency band while power in the 5.2- to 5.6-Hz band remains stable. This increase in power within the 4.0- to 4.5-Hz band is followed by consecutive days of a stable power relationship (box 2) and consistent power within the two frequency bands (indicated by the clustering of power). Following 7 days of a steady power relationship, another transition occurs between box 2 and box 3, with power increasing in the 5.2- to 5.6-Hz band, while power in the 4.0- to 4.5-Hz band changes only slightly. We find that median power clusters between these tremor bands last between 4 and 7 days before switching to a new power relationship. Back azimuth estimates at ETIP (Figure 5b) also experience 3- to 4-day clusters, similar in duration to the power clusters. Power relationship clusters are less defined between the 3.3- to 4.0-Hz and 4.0- to 4.5-Hz frequency bands at ETIP; however, discrete jumps within the relationship are still seen (not shown).

We interpret these observations as the result of a quasi-stable conduit configuration lasting between 3 and 7 days in low hydraulic gradient areas of the subglacial hydrologic system. This hypothesis suggests that multiday conduit evolution occurs in response to changes in water input. While this phenomenon is likely early in the melt season, while conduits are developing (Chu, 2014; Röthlisberger, 1972; Schoof, 2010), we suggest that changes in the relative partitioning of water among different conduits or in the distribution of turbulence-forming obstacles continues during middle to late melt season near ETIP. Several factors of the terminus region may promote this dynamism within the subglacial drainage system, including the low lateral and longitudinal hydraulic gradient of the bed, which do not restrict the location or migration of subglacial conduits, and the anticipated slow water flow, which potentially allows for sediment deposition (section 5.1). Motyka et al. (2006) found that >1 m/year of subglacial sediments are eroded away near the glacier's terminus, which means that, on average, more than 1.9 cm of sediment are eroded per week. Due to the sediment transport occurring near the terminus, reconfiguration of subglacial conduits or changes in the water flow patterns can occur on a weekly time scale.

5.3. Water Input and Tremor Power Relationships

The apparent relationship between tremor and subglacial water flow implies that discharge can be inferred from glaciohydraulic tremor (akin to Gimbert et al., 2014). However, we find that different relationships between water input and tremor power exist for all polarized, Rayleigh wave glaciohydraulic tremor bands. In four out of five cases, higher-frequency signals tend to have lower power for a given discharge than lower-frequency tremor bands (Figure 9) with the exception of the 4.0- to 4.5-Hz band at ETIP, which demonstrates an especially strong power response to discharge. The broad, inverse relationship between frequency and power may be explained by the faster attenuation rate of higher-frequency seismic signals when compared with lower-frequency signals (Battaglia & Aki, 2003; Gimbert et al., 2014; Tsai et al., 2012). The strong power anomaly within the 4.0- to 4.5-Hz band at ETIP may be due to the glacier outlet stream that flows between

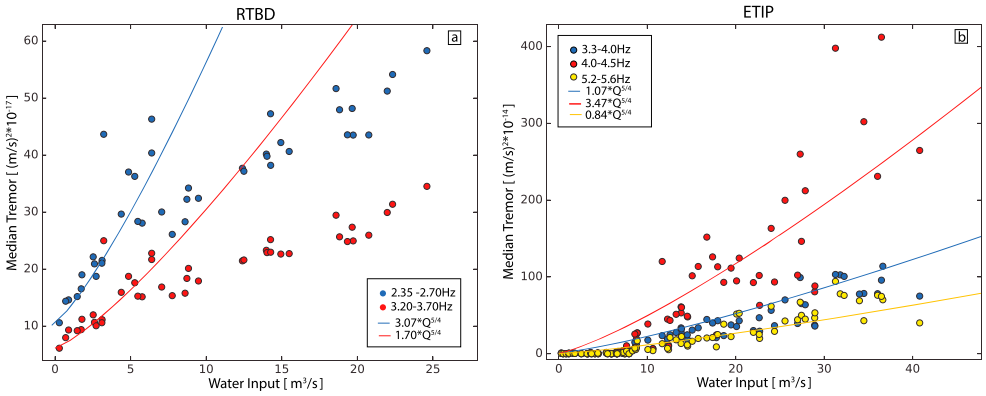

Figure 9. Relationship between water input and the median tremor power at (a) RTBD and (b) ETIP. Each point represents 1 day. The lines represent the $P_w \propto Q^{5/4}$ relationship that is mentioned in Gimbert et al. (2016) with each line having a different scaling factor that is specified in the legend.

ETIP and the glacier and is thus recorded closer to the source. This tremor band switches from Rayleigh wave-dominant to body wave-dominant signals over the course of the melt season, which may indicate that the highest amplitude signal in the 4.0- to 4.5-Hz range switches to a source closer to the seismic station (Figure 3; section 5.4).

To explore the hypothesis that higher frequencies of glaciohydraulic tremor attenuate more strongly than lower frequencies, we use the amplitude decay model outlined in Battaglia and Aki (2003). This model, modified to consider power rather than amplitude decay, holds that

$$P(f) = \frac{P_0}{r^n} e^{-\alpha r}, \tag{14}$$

in which $P(f)$ represents the seismic power of frequency f recorded at a seismic station distance r from the source, P_0 is the seismic power of the source, and n is a geometric factor dependent on the geometrical spreading rate. By assuming that all bands of tremor at a given station are produced in the same location (i.e., r remains constant) and at the same seismic power, P_0, we use the difference between theoretical and actual decay values at each station to identify differences in spatial organization of the conduits. The geometrical spreading rate, n, is not dependent on frequency; thus, this is held fixed throughout the analysis. The anelastic attenuation coefficient of waves with frequency f,

$$\alpha = \frac{\pi f}{Q\beta} \tag{15}$$

is found using the seismic quality factor, Q, and the seismic wave velocity, β, which are dictated by the properties of the medium in which the wave moves.

To analyze the ratio of power decay between different tremor frequencies at a given station, the power decay ratio D

$$D = \ln(P(f_x)) - \ln\left(P\left(f_y\right)\right) = \frac{\pi}{Q\beta}\left(f_y - f_x\right) \tag{16}$$

is found from the division of power recorded in frequencies x and y (equation (14)), where the frequency f represents the median frequency of a given tremor band. The surface wave velocity through glacier ice, β, is estimated to be 1.65 km/s (Mikesell et al., 2012; Röösli et al., 2014), and a quality factor, Q, is estimated to fall between 3.4 and 4. The lower bound of the quality factor estimate has been recorded for low-frequency events on the Cotopaxi volcano ice cap (Metaxian et al., 2003), while the upper bound is the best fitting quality factor for moulin tremor on the Greenland Ice Sheet between 2 and 5 Hz (Röösli et al., 2014). Higher-quality factors have also been identified in some ice sheet settings, but these were calculated with higher-frequency signals and are thus inappropriate for our study (Jones et al., 2013). In the model, we also disregard any signal attenuation at the ice-rock interface since the wavelength of the seismic signal spans the

distance between the ice and seismic station; thus, minimal additional attenuation is expected due to the interface.

The theoretical power decay ratio, D, between the tremor frequency bands of 2.35–2.7 Hz and 3.2–3.7 Hz at RTBD is between 0.44 and 0.52, while the observed average decay ratio is 0.58. At ETIP, the theoretical power decay ratio between the 3.3- to 4.0-Hz and 5.2- to 5.6-Hz bands falls between 0.83 and 0.98, and the observed power decay ratio is 0.43. The powers in the intermediate frequency range at ETIP, near 4.3 Hz, are clearly following a different relationship with water inputs (Figure 9) and are not analyzed using the power decay model. Some of the discrepancy between the theoretical and observed values at both stations can be explained by uncertainties associated with the seismic quality factor, since this value is site specific and may differ slightly from the Q values we selected from the literature.

Based on our power decay ratio analysis, at station RTBD (Figure 9a) where we suggest that single-conduit flow exists, the differing relationship between the two tremor bands seems to be primarily due to faster power decay in higher-frequency signals due to the minimal difference between the expected and calculated decay ratios. While the different frequency bands at RTBD may reflect different source processes or source geometry, our analysis is consistent with a source emitting similar power levels in different frequency bands and from similar distances from the station, that is, results consistent with the assumptions in our model. At ETIP (Figure 9b), where median power comparisons are consistent with multiconduit flow (Figure 6), the difference between the theoretical and observed power decay ratio between frequency bands 3.3–4.0 Hz and 5.2–5.6 Hz is much larger, suggesting that either or both of our assumptions that the tremor bands are produced at the same source location or have the same source power are incorrect. This is consistent with our hypothesis that near-terminus water flow occurs through multiple conduits.

The relationship between power and water input at ETIP and RTBD also both fall within the relationship theorized by Gimbert et al. (2016). Gimbert et al. (2016) states that power from subglacial water flow (P_w) and water discharge (Q) relationships fall between $P_w \propto Q^{5/4}$ and $P_w \propto Q^{14/3}$ depending on how the hydraulic pressure gradient and hydraulic radius of the conduits change in response to varying water fluxes. Power and water input at ETIP and RTBD most closely follow the $P_w \propto Q^{5/4}$ relationship (Figure 9) signifying that power scales with water flow at a constant pressure gradient and that variations in discharge are accommodated by a conduit with varying hydraulic radius (Gimbert et al., 2016) over weekly to monthly time scales. Exploration into shorter time scales may reveal a different relationship between seismic power and subglacial discharge—one in which variations in discharge are accommodated by changes in hydraulic pressure gradients within subglacial conduits (Gimbert et al., 2016).

5.4. Seismic Wave Composition of Glaciohydraulic Tremor

This study also provides new seismological insight into the glaciohydraulic tremor signals themselves. We find that glaciohydraulic tremor on Taku Glacier consists of multiple wave types (Rayleigh waves, body waves, and a mixture of the two; Figure 3). This contradicts the expectation that tremor signals produced by turbulent water flow and bedload transport in rivers are dominated by Rayleigh waves, due to force fluctuations on particles or on the bed (Gimbert et al., 2014; Tsai et al., 2012). Thus, the assumption that water flow produces predominantly Rayleigh wave tremor does not seem to be universally true at Taku Glacier. While we identify body waves in the signal, we cannot estimate the back azimuth direction for these frequency bands using FDPA.

We suggest that the dominant wave type of glaciohydraulic tremor is dictated by the proximity of a seismic station to the source, with signals produced close to seismic stations (within approximately 1 km) predominantly composed of body waves and those from more distant stations largely traveling as Rayleigh waves. Two potential properties of body and surface waves lend support for this hypothesis. First, body wave power attenuates faster than surface wave power, with the energy or power of body waves decaying at $1/r^2$ and the power of surface waves decaying at $1/r$, where r is the distance between station and source (Stein & Wysession, 2003, p. 86). Thus, body waves may dominate a glaciohydraulic tremor frequency in situations where they have not attenuated significantly, suggesting the source is closer to the station than Rayleigh wave-dominated frequencies. ETIP exhibits six distinct bands of body wave glaciohydraulic tremor, while RTBD is solely dominated by Rayleigh wave tremor (Figure 3), which is consistent with ETIP being in closer proximity to its seismic sources than RTBD.

Second, the distance between a seismic station and tremor source also dictates if a seismic wave has had sufficient travel distance to produce the constructive interference between *P* and *SV* waves at the Earth's surface necessary to generate Rayleigh waves (Stein & Wysession, 2003, p. 86). Near-field sources, which we define as sources within one wavelength of the seismometer, are not able to form defined Rayleigh waves due to insufficient interference between *P* and *SV* waves. If we assume seismic wave velocities of 1.65 km/s (appropriate for high-frequency Rayleigh waves moving through ice) within the 1.5- to 10-Hz range (Mikesell et al., 2012; Röösli et al., 2014), wavelengths (and the threshold for near-field sources) are between 0.17 and 1.1 km, with longer wavelengths associated with lower frequencies. At ETIP, which shows prominent bands of body wave tremor (Figure 3), there are both near-field glacial and terrestrial river sources that may produce distinct body wave bands. However, at RTBD, where subglacial water likely flows at the center of the glacier (as directed by steep lateral gradients), the tremor source is ~2.3 km away from the seismic station, which is greater than the maximum near-field source estimate. This provides a second possible explanation as to why there are no body wave tremor bands at RTBD (Figure 3).

Surface waves travel trapped against and interact with the traction-free Earth surface. Beyond some critical source depth, the Earth is no longer sensitive to this free surface and surface wave particle motions decay exponentially toward 0 (Stein & Wysession, 2003, p. 89). For the wavelengths calculated above, the critical source depth for Rayleigh waves is between 0.23 and 1.7 km (about 1.5 times the wavelength of the seismic signal), which are similar to or exceed measured glacier thicknesses (Motyka et al., 2006). Therefore, surface waves can be produced even at the bed of Taku Glacier.

5.5. Frequency Structure and Propagation of Rayleigh Wave Glaciohydraulic Tremor

While increased seismic power exists across a broad range of frequencies on Taku Glacier, the strongest power increases composed of polarized, Rayleigh waves fall between 1.5 and 10 Hz (Figure 3), which is consistent with the findings of Bartholomaus et al. (2015) on Yahtse Glacier, Mendenhall Glacier, Columbia Glacier, and Jakobshavn Isbræ, as well as the tremor frequencies produced by terrestrial rivers (Burtin et al., 2008; Gimbert et al., 2014; Schmandt et al., 2013, 2017; Tsai et al., 2012). Like the power density spectra in Burtin et al. (2008) and Schmandt et al. (2013), glaciohydraulic tremor exhibits as multiple distinct power peaks within this 1.5- to 10-Hz range. The quantity and frequency ranges of polarized, Rayleigh wave glaciohydraulic tremor power peaks are not consistent between seismic stations (Figure 3); thus, we see no clear, diagnostic seismic signatures of glaciohydraulic tremor.

A previously unreported feature of glaciohydraulic tremor is that distinct frequency bands propagate from the same source direction, as seen in Figure 4. While we have no conclusive explanations for this phenomenon, we suggest that the superposition of turbulence from different-sized flow obstructions or subglacial water flow through neighboring conduits may be plausible hypotheses. Turbulent water flow, which is a mechanism proposed for the generation of terrestrial river tremor (Gimbert et al., 2014; Tsai et al., 2012) creates a broad spectrum of eddy sizes, with obstacles in the water flow producing eddies at all sizes smaller than the obstacle itself (Kolmogorov, 1941). Momentum within large turbulent eddies dissipates through energy transfer to ever smaller eddies according to a well-defined power law and large obstacles give off a broader range of eddy sizes than smaller obstacles can. Thus, we envision a conduit in which a large obstacle produces a broad spectrum of seismic energy at frequencies greater than its scale-appropriate minimum, while smaller obstacles produce additional seismic energy at frequencies greater than a higher cutoff value. The site-specific sizes of subglacial water flow obstacles as well as their proximity to one another may lead to tremor production with a range of site-specific dominant frequencies. We also suggest that, in low hydraulic gradient areas where multiconduit flow likely occurs, such as ETIP, water flowing through neighboring conduits with different diameters may lead to seismic tremor propagating from the same source direction.

The propagation distance of polarized, Rayleigh wave glaciohydraulic tremor can also be determined from our analysis due to the varying dates of tremor initiation between seismic stations on Taku Glacier (Figure S3). The tremor signal that started at ETIP on 1 June near the terminus is not recorded by either RTBD or TWLV, which signifies that these signals can only be detected locally. This same phenomenon occurs between RTBD and TWLV, with the tremor at RTBD not recorded by station TWLV. If we assume

the polarized, Rayleigh wave glaciohydraulic tremor signal recorded at RTBD comes from the center of the glacier to the southeast of RTBD (Figure 4d), the signal travels ~2 km to RTBD but not the 6 km that is needed to reach station TWLV. Thus, polarized, Rayleigh wave glaciohydraulic tremor at Taku Glacier can be recorded at up to 2- to 6-km distances during midsummer.

6. Conclusions

This study provides new insight into the organization of subglacial water systems as well as the time scales of conduit evolution and migration. We suggest that single-conduit and multiconduit flow can be detected through time series analysis of Rayleigh wave back azimuths, tremor power comparisons, and water input-power relationships. Theoretical analysis indicates that the structural pattern of this flow is influenced by the subglacial hydraulic potential gradient. Tremor signals produced in low potential gradient areas experience abrupt jumps between quasi-stable configurations that last between 3 and 7 days. We hypothesize that these changes occur due to changes in water routing between neighboring conduits. Tremor produced in higher potential gradient areas remains relatively stationary throughout the melt season. Comparison of subglacial discharge with glaciohydraulic tremor signals at each station suggests that sustained water input to the subglacial water system is needed to produce polarized, Rayleigh wave glaciohydraulic tremor. Once formed, these conduits appear stable for the remainder of the summer, at least for the duration of our observations: mid-July at stations ETIP and RTBD and through early September at TWLV. We also show that the relationship between tremor power and subglacial water flow is dependent on the frequency of tremor, with high frequencies potentially affected by greater attenuation rates.

Our study also explores previously unreported qualities of glaciohydraulic tremor wave composition, propagation, and frequency structure. We find that glaciohydraulic tremor is composed of multiple wave types (Rayleigh waves, body waves, and mixed waves), which contradicts the assumption from research on terrestrial rivers that all tremor signals are dominated by Rayleigh waves (Gimbert et al., 2014; Tsai et al., 2012). We also suggest that polarized, Rayleigh wave glaciohydraulic tremor propagates no further than 2–6 km during midsummer. We find that tremor on the glacier shows no clear, diagnostic spectral signatures, with the exception that glaciohydraulic tremor occurs within the previously reported 1.5- to 10-Hz band. Multiple, distinct, spectral peaks in glaciohydraulic tremor seismic power propagate from the same source direction.

Seismology provides a continuous method to monitor subglacial water flow and the evolution of the subglacial water system. Improving water input estimates by tracking runoff contributions from snowmelt and applying empirical constraint on our melt model will increase the accuracy of estimated tremor-water input relationships. Furthermore, a denser network of seismometers, in locations far from terrestrial water flow, will also allow for better spatial resolution in tracking temporal changes in tremor. Future research into the relationship between glaciohydraulic tremor and subglacial water flow using global positioning systems (GPSs) and ground penetrating radar (GPR) may enhance our understanding of the relationship between glacier motion and the spatiotemporal change of the subglacial water system. These instruments can also be used to create hydropotential maps of the glacier bed and may lead to more precise subglacial conduit locations, an increased understanding of subglacial water flow patterns, and a better quantification of local glacier dynamics.

Acknowledgments

Raw seismic data described in this paper are available through the Incorporated Research Institutions for Seismology Data Management Center (http://ds.iris.edu/mda/ZQ?timewindow=2015-2016; Amundson et al., 2015). The raw weather data used in this paper can be found through the Arctic Data Center (https://doi.org/10.18739/A2H98ZC7V; Bartholomaus & Walter, 2018). Python code developed to carry out the analyses presented here is available at https://github.com/voremargot/Seismic-Tremor-Reveals-Spatial-Organization-and-Temporal-Changes-of Subglacial-Water-System and https://github.com/tbartholomaus/med_spec. This study was made possible with support from the University of Texas Institute for Geophysics and the University of Idaho. We thank Ginny Catania for the loan of weather stations. J. P. W.'s and J. M. A.'s contributions to this work were supported by the U.S. National Science Foundation (OPP-1337548 and OPP-1303895). T. C. B. thanks Dylan Mikesell for an early conversation, which inspired the analysis presented here.

References

Amundson, J., Bartholomaus, T., Walter, J., & Winberry, P. (2015). Taku Glacier, International Federation of Digital Seismograph Networks, Other/Seismic Network. https://doi.org/10.7914/SN/ZQ_2015

Aso, N., Tsai, V. C., Schoof, C., Flowers, G. E., Whiteford, A., & Rada, C. (2017). Seismologically observed spatiotemporal drainage activity at moulins. *Journal of Geophysical Research: Solid Earth*, *122*, 9095–9108. https://doi.org/10.1002/2017JB014578

Bartholomaus, T. C., Amundson, J. M., Walter, J. I., O'Neel, S., West, M. E., & Larsen, C. F. (2015). Sublacial discharge at tidewater glaciers revealed by seismic tremor. *Geophysical Research Letters*, *42*, 6391–6398. https://doi.org/10.1002/2015GL064590

Bartholomaus, T. C., Anderson, R. S., & Anderson, S. P. (2008). Response of glacier basal motion to transient water storage. *Nature Geoscience*, *1*(1), 33–37. https://doi.org/10.1038/ngeo.2007.52

Bartholomaus, T. C., & Walter, J. (2018). *Weather data during the 2016 melt season at Taku Glacier*. Alaska: Arctic Data Center. https://doi.org/10.18739/A2H98ZC7V

Bartholomew, I., Nienow, P., Mair, D., Hubbard, A., King, M. A., & Sole, A. (2010). Seasonal evolution of subglacial drainage and acceleration in a Greenland outlet glacier. *Nature Geoscience*, *3*(6), 408–411. https://doi.org/10.1038/ngeo863

Battaglia, J., & Aki, K. (2003). Location of seismic events and eruptive fissures on the Piton de la Fournaise volcano using seismic amplitudes. *Journal of Geophysical Research*, *108*(B8), 2364–2378. https://doi.org/10.1029/2002JB002193

Burtin, A., Bollinger, L., Vergne, J., Cattin, R., & Nábělek, J. L. (2008). Spectral analysis of seismic noise induced by rivers: A new tool to monitor spatiotemporal changes in stream hydrodynamics. *Journal of Geophysical Research*, *113*, B05301. https://doi.org/10.1029/2007JB005034

Chu, V. W. (2014). Greenland ice sheet hydrology: A review. *Progress in Physical Geography*, *38*(1), 19–54. https://doi.org/10.1177/0309133313507075

Cowton, T., Nienow, P., Sole, A., Wadham, J., Lis, G., Bartholomew, I., et al. (2013). Evolution of drainage system morphology at a land-terminating Greenlandic outlet glacier. *Journal of Geophysical Research: Earth Surface*, *118*, 29–41. https://doi.org/10.1029/2012JF002540

Creyts, T. T., Clarke, G. K. C., & Church, M. (2013). Evolution of subglacial overdeepenings in response to sediment redistribution and glaciohydraulic supercooling. *Journal of Geophysical Research: Earth Surface*, *118*, 423–446. https://doi.org/10.1002/jgrf.20033

Flowers, G. E. (2008). Subglacial modulation of the hydrograph from glacierized basins. *Hydrological Processes*, *22*(19), 3903–3918. https://doi.org/10.1002/hyp.7095

Fountain, A. G., & Walder, J. S. (1998). Water flow through temperate glaciers. *Reviews of Geophysics*, *36*(3), 299–328. https://doi.org/10.1029/97RG03579

Gimbert, F., Tsai, V. C., Amundson, J. M., Bartholomaus, T. C., & Walter, J. I. (2016). Subseasonal changes observed in subglacial channel pressure, size, and sediment transport. *Geophysical Research Letters*, *43*, 3786–3794. https://doi.org/10.1002/2016GL068337

Gimbert, F., Tsai, V. C., & Lamb, M. P. (2014). A physical model for seismic noise generation by turbulent flow in rivers. *Journal of Geophysical Research: Earth Surface*, *119*, 2209–2238. https://doi.org/10.1002/2014JF003201

Goodling, P. J., Lekic, V., & Prestegaard, K. (2018). Seismic signature of turbulence during the 2017 Oroville Dam spillway erosion crisis. *Earth Surface Dynamics*, *6*(2), 351–367. https://doi.org/10.5194/esurf-6-351-2018

Hewitt, I. J. (2011). Modelling distributed and channelized subglacial drainage: The spacing of channels. *Journal of Glaciology*, *57*(202), 302–314. https://doi.org/10.3189/002214311796405951

Hock, R. (2003). Temperature index melt modelling in mountain areas. *Journal of Hydrology*, *282*(1-4), 104–115. https://doi.org/10.1016/S0022-1694(03)00257-9

Iken, A., & Bindschadler, R. A. (1986). Combined measurements of subglacial water pressure and surface velocity of Findelengletscher, Switzerland: Conclusions about drainage system and sliding mechanism. *Journal of Glaciology*, *32*(110), 101–119. https://doi.org/10.1017/S0022143000006936

Jones, G. A., Kulessa, B., Doyle, S. H., Dow, C. F., & Hubbard, A. (2013). Automated approach to the location of icequakes using seismic waveform amplitudes. *Annals of Glaciology*, *54*(64). https://doi.org/10.3189/ 2013AoG64A074

Kienholz, C., Herreid, S., Rich, J. L., Arendt, A. A., Hock, R., & Burgess, E. W. (2015). Derivation and analysis of a complete modern-date glacier inventory for Alaska and Northwest Canada. *Journal of Glaciology*, *61*(227), 403–420. https://doi.org/10.3189/2015JoG14J230

Kolmogorov, A. (1941). The local structure of turbulence in incompressible viscous fluid for very large Reynolds numbers. *Doklady Akademii Nauk SSSR*, *30*(4), 299–303.

Koper, K., & Hawley, V. (2010). Frequency dependent polarization analysis of ambient seismic noise recorded at broadband seismometers in the Central United States. *Earthquake Science*, *23*(5), 439–447. https://doi.org/10.1007/s11589-010-0743-5

Koper, K. D., & Burlacu, R. (2015). The fine structure of double-frequency microseisms recorded by seismometers in North America. *Journal of Geophysical Research: Solid Earth*, *120*, 1677–1691. https://doi.org/10.1002/2014JB011820

Larsen, C. F., Motyka, R. J., Arendt, A. A., Echelmeyer, K. A., & Geissler, P. E. (2007). Glacier changes in Southeast Alaska and Northwest British Columbia and contribution to sea level rise. *Journal of Geophysical Research*, *112*, F01007. https://doi.org/10.1029/2006JF000586

Metaxian, J. P., Araujo, S., Mora, M., & Lesage, P. (2003). Seismicity related to the glacier of Cotopaxi Volcano, Ecuador. *Geophysical Research Letters*, *30*(9), 1483. https://doi.org/10.1029/2002GL016773

Mikesell, T. D., van Wijk, K., Haney, M. M., Bradford, J. H., Marshall, H. P., & Harper J. T. (2012) Monitoring glacier surface seismicity in time and space using Rayleigh waves. *Journal of Geophysical Research, 117*, F02020. https://doi.org/10.1029/2011JF002259

Motyka, R. J., Truffer, M., Kuriger, E. M., & Bucki, A. K. (2006). Rapid erosion of soft sediments by tidewater glacier advance: Taku Glacier Alaska, USA. *Geophysical Research Letters*, *33*, L24504. https://doi.org/10.1029/2006GL028467

Nolan, M., Motyka, R. J., Echelmeyer, K., & Trabant, D. C. (1995). Ice-thickness measurements of Taku Glacier, Alaska, U.S.A., and their relevance to its recent behavior. *Journal of Glaciology*, *41*(139), 541–553. https://doi.org/10.1017/S0022143000034870

Park, J., Vernon, F. L., & Lindberg, C. R. (1987). Frequency dependent polarization analysis of high-frequency seismograms. *Journal of Geophysical Research*, *92*(B12), 12,664–12,674. https://doi.org/10.1029/JB092iB12p12664

Pelto, M. S., Miller, M. M., Adema, G. W., Beedle, M. J., McGee, S. R., Sprenke, K. F., & Lang, M. (2008). The equilibrium flow and mass balance of the Taku Glacier, Alaska, 1950-2006. *The Cryosphere*, *2*(2), 147–157. https://doi.org/10.5194/tc-2-147-2008

Post, A., & Motyka, R. J. (1995). Taku and Le Conte Glaciers, Alaska: Calving-speed control of late-Holocene asynchronous advances and retreats. *Physical Geography*, *16*(1), 59–82. https://doi.org/10.1080/02723646.1995.10642543

Röösli, C., Walter, F., Husen, S., Andrews, L. C., Lüthi, M. P., Catania, G. A., & Kissling, E. (2014). Sustained seismic tremors and icequakes detected in the ablation zone of the Greenland ice sheet. *Journal of Glaciology*, *60*(221), 563–575. https://doi.org/10.3189/2014joG13j210

Röthlisberger, H. (1972). Water pressure in intra- and subglaical channels. *Journal of Glaciology*, *11*(62), 177–203.

Rost, S., & Thomas, C. (2002). Array seismology: Methods and applications. *Reviews of Geophysics*, *40*(3), 1008. https://doi.org/10.1029/2000RG000100

Roth, D. L., Finnegan, N. J., Brodsky, E. E., Rickenmann, D., Turowski, J. M., Badoux, A., & Gimbert, F. (2017). Bed load transport and boundary roughness changes as competing causes of hysteresis in the relationship between river discharge and seismic amplitude recorded near a steep mountain stream. *Journal of Geophysical Research: Earth Surface*, *122*, 1182–1200. https://doi.org/10.1002/2016JF004062

Schmandt, B., Aster, R. C., Scherler, D., Tsai, V. C., & Karlstrom, K. (2013). Multiple fluvial processes detected by riverside seismic and infrasound monitoring of a controlled flood in the Grand Canyon. *Geophysical Research Letters*, *40*, 4858–4863. https://doi.org/10.1002/grl.50953

Schmandt, B., Gaeuman, D., Stewart, R., Hansen, S. M., Tsai, V. C., & Smith, J. (2017). Seismic array constraints on reach-scale bedload transport. *Geology*, *45*(4), 299–302. https://doi.org/10.1130/G38639.1

Schoof, C. (2010). Ice-sheet acceleration driven by melt supply variability. *Nature*, *468*(7325), 803–806. https://doi.org/10.1038/nature09618

Shelly, D. R., Beroza, G. C., & Ide, S. (2007). Non-volcanic tremor and low-frequency earthquake swarms. *Nature*, *446*(7133), 305–307. https://doi.org/10.1038/nature05666

Shreve, R. L. (1972). Movement of water in glaciers. *Journal of Glaciology*, *11*(62), 205–214. https://doi.org/10.1017/S002214300002219X

Stein, S., & Wysession, M. (2003). *An introduction to seismology, earthquakes, and Earth structure*. Oxford, UK: Blackwell Publishing.

Tsai, V. C., Minchew, B., Lamb, M. P., & Ampuero, J.-P. (2012). A physical model for seismic noise generation from sediment transport in rivers. *Geophysical Research Letters*, *39*, L02404. https://doi.org/10.1029/2011GL050255

Walter, F., Roux, P., Roeoesli, C., Lecointre, A., Kilb, D., & Roux, P.-F. (2015). Using glacier seismicity for phase velocity measurements and Green's function retrieval. *Geophysical Journal International*, *201*(3), 1722–1737. https://doi.org/10.1093/gji/ggv069

Werder, M. A., Hewitt, I. J., Schoof, C. G., & Flowers, G. E. (2013). Modeling channelized and distributed subglacial drainage in two dimensions. *Journal of Geophysical Research: Earth Surface*, *118*, 2140–2158. https://doi.org/10.1002/jgrf.20146

Willis, I. C. (1995). Intra-annual variations in glacier motion: A review. *Progress in Physical Geography*, *19*(1), 61–106. https://doi.org/10.1177/030913339501900104

Winberry, J. P., Anandakrishnan, S., & Alley, R. B. (2009). Seismic observations of transient subglacial water-flow beneath MacAyeal Ice Stream, West Antarctica. *Geophysical Research Letters*, *36*, L11501. https://doi.org/10.1029/2009GL037730

Workman, E., Lin, F.-C., & Koper, K. D. (2016). Determination of Rayleigh wave ellipticity across the Earthscope Transportable Array using single-station and array-based processing of ambient seismic noise. *Geophysical Journal International*, *208*(1), 234–245. https://doi.org/10.1093/gji/ggw381